

Towards Subsurface Stress and Strain Monitoring and Modeling at Geothermal Fields -- a Case Study of the Patua Geothermal Field

Nori Nakata¹, Chet Hopp¹, Linqing Luo¹, Hongrui Qiu¹, Don W. Vasco¹, Harry Lisabeth¹, Torquil Smith¹, Eric Sonnenthal¹, Michelle Robertson¹, Michael Swyer²

¹Lawrence Berkeley National Laboratory, ²Cyrq Energy

Keywords

structural monitoring, seismicity, stress and strain, seismic, geodesy, THMC modeling

ABSTRACT

Geothermal fields often exhibit abundant microseismicity and surface deformation, both from natural tectonic/hydrologic forces and associated with reservoir injection/production and shallow groundwater pumping. Our study of the Patua Geothermal Field combines seismic observations and analysis of micro-earthquakes and ambient noise, surface deformation (InSAR and GPS), laboratory measurements, and numerical modeling to characterize subsurface stress and strain and predict the Thermal-Hydrological-Mechanical (THM) behavior of the reservoir. We are also developing advanced fiber-optic sensing systems for convenient monitoring of geothermal fields.

At the field, we have recorded continuous seismic motion at five shallow boreholes, where we have bottomhole and surface stations, for monitoring microearthquakes since June 2021. This local array lowers the magnitude completeness of earthquake detection, enabling us to characterize fault distribution and their criticalness. These sensors also record ambient-noise data for detecting time-lapse changes of subsurface velocities using coda-wave interferometry. Time-lapse changes in velocities provide a unique view of subsurface elastic changes between each receiver pair. By utilizing laboratory-calibrated dynamic moduli, changes in velocity can be linked to the geomechanical state of the reservoir. These experiments also provide insights into aseismic deformation, which plays an important role in earthquake nucleation but is challenging to measure in the field. Surface deformation estimated from InSAR shows a clear trend of subsidence, in addition to the annual cycle induced by hydrological changes. The cumulative deformation from 2018 to 2022, as well as inversion results, indicate volume changes in the reservoir. We compare the results of seismic and surface deformation to analyze subsurface stress changes.

1. Introduction

Understanding the detailed stress and strain states in the reservoir and surrounding structure is crucial for mitigating large induced seismicity and reservoir management in geothermal fields.

This is especially important when we increase the usage of geothermal resources. In this study, we demonstrate the characterization of stress states at the Patua geothermal field in Nevada (Combs et al., 2012; Garg et al., 2015; Murphy et al., 2017; Cladouhos et al., 2017; Pollack et al., 2021) by combining seismic observations, structural monitoring with seismic and geodesy data, and Thermal-Hydrological-Mechanical-Chemical (THMC) modeling. We combine data-driven and physics-based approaches for understanding the subsurface stress. The seismic observation and ambient noise analysis provide subsurface S-wave velocities (V_s) at each depth and their time-lapse changes. Surface waves reconstructed from cross correlations of ambient noise recordings from pairs of seismic sensors are used to invert a 1-D V_s profile at the Patua site. Coda wave interferometry is used to infer temporal changes of seismic velocities beneath the sensors. The low-wavenumber surface deformation obtained by InSAR is related to physical changes in the reservoir, and we estimate volume changes by inverting the deformation. The THMC modeling can numerically model the subsurface fluid flow and stress changes (Smith et al., 2023). In this study, we present results from each analysis and discuss how we can combine them for more comprehensive monitoring of subsurface stress and strain states.

2. Seismic Observations

From July 2012 until the end of 2013, a seismic network of 18 borehole-installed 15-Hz geophones was operated at Patua. Most of the equipment was removed after 2013, but many of the geophones were either permanently grouted in place, or were left locked in the boreholes. In June of 2021, in preparation for new DOE-funded projects set to begin at Patua, a team from Lawrence Berkeley National Laboratory (LBNL) began reinstalling recording equipment at many of these sites and testing the functionality of the preexisting downhole geophones. At each site, we also installed a 2-Hz geophone near the wellhead to help characterize the attenuation properties of the surface sediments covering the reservoir. From June 2021 to March 2023, we recorded data from six of the original 18 sensors and found five to still be functioning (Figure 1). Data were recorded continuously at 500 Hz for both the surface and downhole geophones at each site. Due to issues with snow-covered solar panels and faulty recorders, a minimum of four and maximum of five sites were operational at any one time throughout the dataset. The downhole sensor at site 4509, while functioning, is suspected to be poorly coupled and have multiple bad components, so the recording equipment was relocated to site 23A-17 in January 2022. All other borehole sensors appear to be functioning normally.

The first priority of the seismic network at Patua is to detect and precisely locate as many earthquakes as possible. The more seismicity the network can detect, the better it is able to help mitigate the risk of larger-magnitude events and the more completely it can illuminate seismically active structures in the reservoir. These structures are often key features of the reservoir model as they often serve as either flow pathways or flow baffles and are therefore critical to identify. The Patua network, when using up to 18 borehole sensors, had a magnitude of completeness of roughly 0.0, meaning that it was able to detect all seismicity with a magnitude of >0.0 (or slip on a fracture with a radius of ~ 5 -10 m).

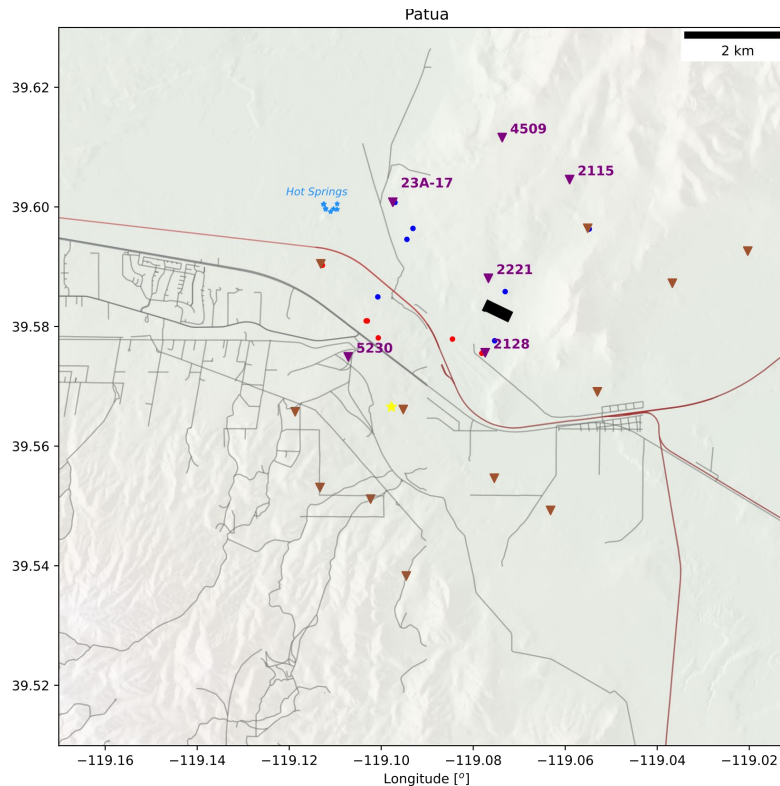


Figure 1: Overview of the Patua geothermal field indicating the locations of previous seismic network sites (brown triangles) and sites that have been reoccupied at some point in the last two years (purple triangles). The location of the proposed stimulation well is shown as a yellow star and the power plant is shown as a black rectangle. Red and blue dots signify production and injection boreholes respectively.

3. Seismic Ambient Noise Analysis

We analyze continuous recordings from five pairs of co-located surface and shallow-borehole seismometers deployed at the Patua geothermal field between June 2021 and May 2023. The ambient-noise data recorded by this local array is used to measure time-lapse changes of subsurface velocities using coda-wave interferometry. To do so, we first preprocess the daily recording following the procedure of Bensen et al. (2007). Figure 2 shows the preprocessing procedure for a vertical recording on a specific day from an example of station 2221. Note that the amplitudes for waves recorded at the low frequency band (0.1-1 Hz) are much (~ 3 orders of magnitude) smaller than those at the high frequency band (1-10 Hz). Thus, we preprocess the data for the low (0.1-1 Hz) and the high (1-10 Hz) frequency bands, separately.

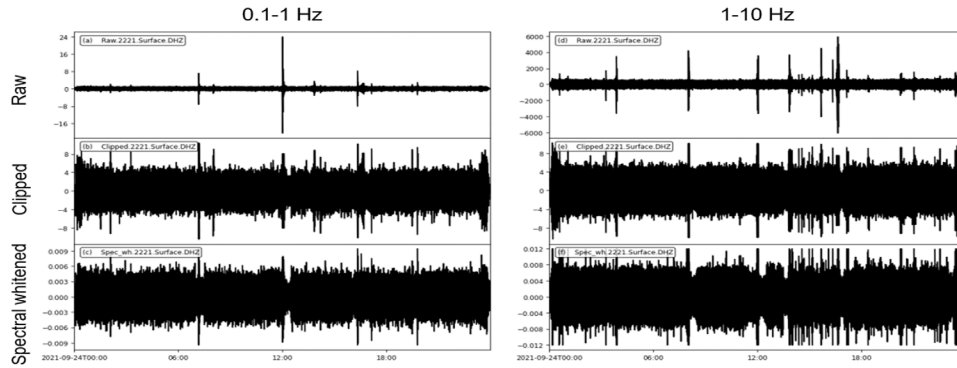


Figure 2: The vertical component daily recording at 2021-09-24 for station 2221 filtered at (a) 0.1-1 Hz and (d) 1-10 Hz. Following the procedure of Bensen et al. (2007), clipping (b, e) and spectral whitening (c, f) are applied to the filtered continuous recording before coda wave interferometry. A 30-min-long moving window is used in the preprocessing.

Figure 3 demonstrates the amplitude spectra of every 5-min-long window of the data before (top) and after (bottom) the spectral whitening. The amplitude spectra show certain shapes in both the low and high frequency bands. This is particularly clear for the high frequency band, where several strong peaks are observed between 4-6 Hz. The observed pattern may relate to either the excitation mechanism of the noise sources or the local structure beneath the station (e.g., reflections from horizontal interfaces) or both. Such a pattern can potentially be used to constrain structures of the shallow materials or properties of ambient noise sources at Patua. Since the focus of this study is to monitor changes in subsurface velocities, we suppress such patterns via spectral whitening.

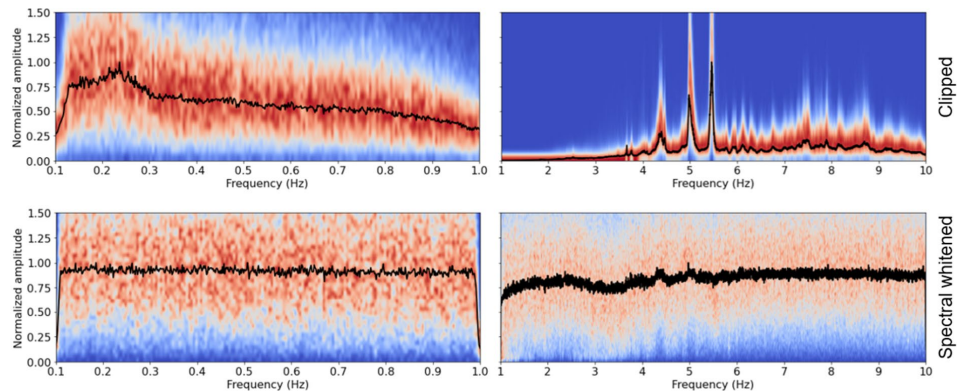


Figure 3: Amplitude-frequency probability density maps of data shown in Figure 2 at low (left) and high (right) frequency bands. Results computed for data before and after the spectral whitening are shown in the top and bottom panels, respectively. Warmer colors indicate larger amplitudes. The black curve illustrates the mean of all the amplitude spectra.

We then cross correlate the preprocessed daily recordings for each station pair and component combination. Figure 4 shows the data coverage for different stations. Considering stations 2115 and 2317 only provide data for less than a year, we only focus on the analysis of data recorded by stations 2128, 2221, and 5230 in this study. Since each borehole has both surface and borehole stations, we compute daily ambient noise cross correlations (ANCs) for pairs of borehole stations and co-located borehole and surface stations, but only in the high frequency band (1-10 Hz), as borehole stations are 15-Hz sensors. As a test, Figure 5 illustrates the daily ANCs computed for

an example station pair 2128-2221 at vertical-vertical (ZZ) component for about one year. Clear and coherent coda waves are observed in daily ANC's at the high frequency band (> 1 Hz), whereas the coda waves at the low frequency band (< 1 Hz) are much noisier. Further analysis suggests that the low frequency ANC's cannot provide reliable measurements of changes in coda wave travel times, even after stacking over 21 days and applying a denoising filter (Figure 6). Therefore, we do not extend the calculation and analysis of coda waves at frequencies < 1 Hz to the whole dataset.

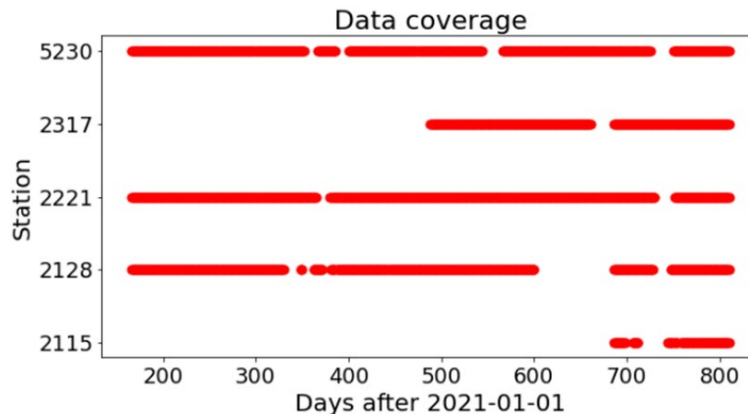


Figure 4: Data coverage of the analyzed seismic network.

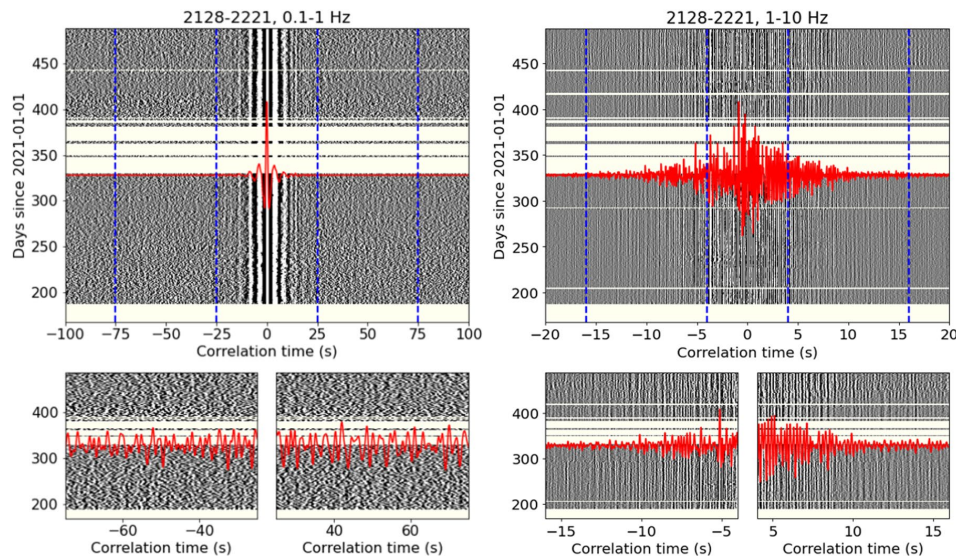


Figure 5: Daily ambient noise cross correlations (ANCs) for station pair 2128-2221 over the entire recording period computed for the low (left) and high (right) frequency bands. The coda waves used to detect subsurface velocity changes are outlined by the blue dashed lines and zoomed in at the bottom panels.

In the next step, we estimate relative travel time changes (dt/t) using the time-domain stretching method (Lobkis and Weaver 2003) for coda waves above 1 Hz over the entire ~ 2 -year-long recording period. The stretching method dilates or compresses a test trace to fit with a reference trace in the time domain and assumes that temporal perturbations in coda wave travel times are small. Figure 7 demonstrates the calculation of dt/t for coda waves narrow bandpass filtered between 2-6 Hz using the example station pair (2128-2221) at the ZZ component. Although the

coda waves filtered between 2-6 Hz are visually coherent, we still observe clear incoherence noise (Figs. 7c-d) that increases the uncertainty of dt/t measurements (Fig. 7b). Here, we denoise the coda waves using a well-developed SVD-based Wiener filter (Moreau et al. 2017). After denoising, the signal-to-noise ratio of coda waves is much higher (Figs. 7g-h), resulting in higher coherence values (Fig. 7e) and smaller uncertainty values (Fig. 7f).

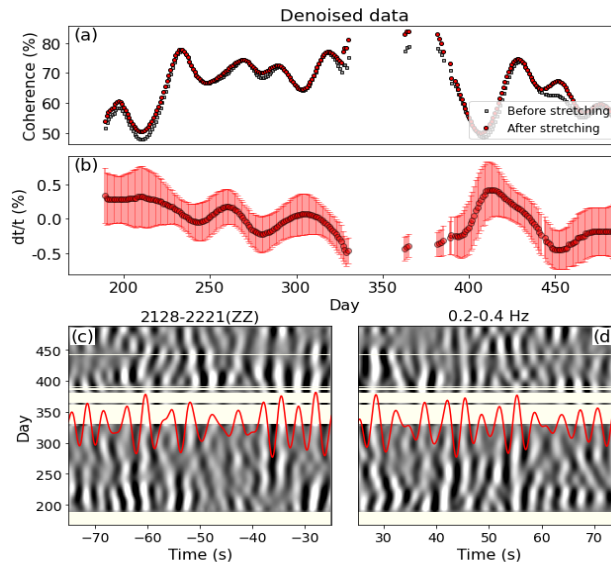


Figure 6: dt/t measured using coda waves filtered at a low frequency band (0.2-0.4 Hz). The bottom panels display the coda waves at both positive and negative time lags, whereas the top panels illustrate the coherence and dt/t measured by comparing each daily ANC with the mean.

We note that dt/t can be measured using coda waves computed for different combinations of station pairs, components, and frequency bands. Since there are hundreds of dt/t curves, we first compare the results computed for different frequency bands using the example surface station pair 2128-2221. As shown in Figure 8a, the dt/t varies within a $\sim 1\%$ range and a long-term trend of $\sim 0.5\%$ velocity decrease per year ($dt/t = -dv/v$) that are only observed in dt/t measured at the lower frequency band (1-3 Hz). This likely indicates that the observed velocity changes occurred at a depth range below the sensitivity of the coda waves at frequencies higher than 3 Hz recorded by surface stations. We confirm the long-term trend in dt/t measured at 1-3 Hz is robust by verifying that it can be seen from coda waves at multiple components (Fig. 8b), station pairs (Fig. 8c), and in borehole stations (Fig. 8d). It is interesting to note that, although much smaller ($\sim 0.1\%$ per year), the dt/t curve at 4-10 Hz has a linear trend of velocity increase, especially for those obtained from borehole stations (Fig. 8f). Such reversals in the long-term trend of dt/t obtained at different frequency bands are also seen from other station pairs (not shown here) and suggests that velocities in subsurface structures likely increase at shallow depth (high frequency) and then decrease below certain depth (low frequency).

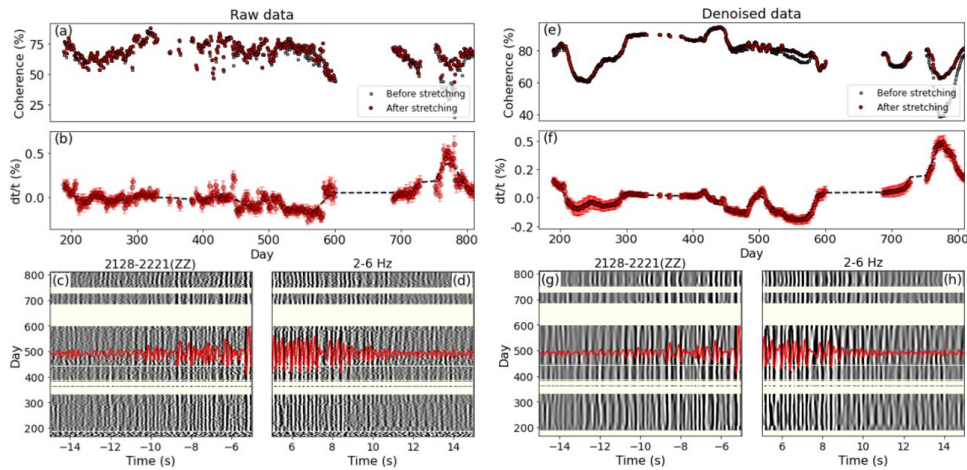


Figure 7: Relative travel time changes (dt/t) measured using coda waves before (left) and after (right) denoising. The bottom panels display the coda waves at both positive and negative time lags, whereas the top panels illustrate the coherence and dt/t measured by comparing each daily ANC with the mean.

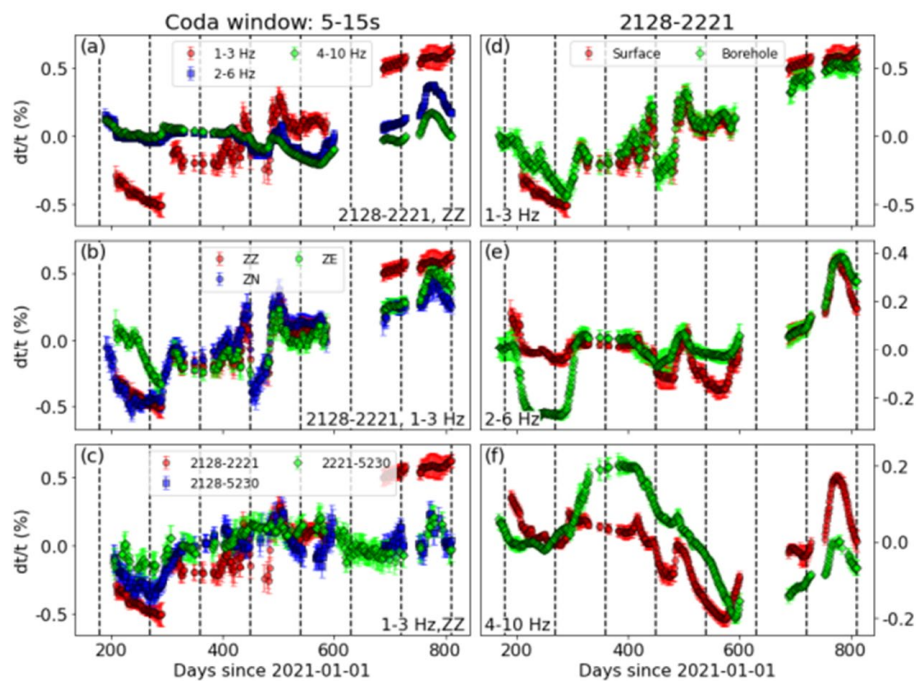


Figure 8: Comparative analysis of dt/t curves measured using coda waves at the high frequency band (1-10 Hz) for (a) different frequency bands, (b) components, and (c) station pairs. (d)-(f) show the comparison between dt/t obtained from surface (red) and borehole (green) stations.

To better understand the depth distribution of observed temporal changes in seismic velocities, we first measure the group velocity dispersion of Rayleigh waves extracted from ANCs computed from all available station pairs (left panel of Fig. 9). Then, the group velocity dispersion is used to invert for an average 1-D shear wave velocity (V_s) profile beneath the Patua geothermal region (right panel of Fig. 9) via Neighborhood algorithm (Wathelet, 2008). The 1-D V_s profiles that fit the dispersion data well (gray shaded area in the right panel of Fig. 9) all show a sharp velocity gradient in the top ~ 200 m followed by a second step velocity gradient from 400 m to 1 km.

Assuming coda waves are dominated by surface wave energy, we can estimate the depth sensitivity of dt/t obtained from coda waves for different frequencies and Figure 10 shows the sensitivity kernels for several frequencies between 1-4 Hz. While dt/t obtained from coda waves at frequencies lower than or around 1 Hz are affected by velocity structures below 500 m (e.g., geothermal reservoirs), coda waves at frequencies higher than 2 Hz are only sensitive to structures above 500 m. Combined with Figure 10, the long-term linear trend in dt/t likely suggests that velocities are generally increasing in the top 200 m (> 4 Hz) and decreasing below 300 m (1-3 Hz). Apart from long-term linear trends, seasonal variations with amplitudes that increase with frequency (i.e., decrease with depth) are also seen in dt/t curves, suggesting it is likely induced by surface loadings (e.g., thermoelastic strain, precipitation). In addition, we also see cycles with shorter intervals (about one month) in dt/t .

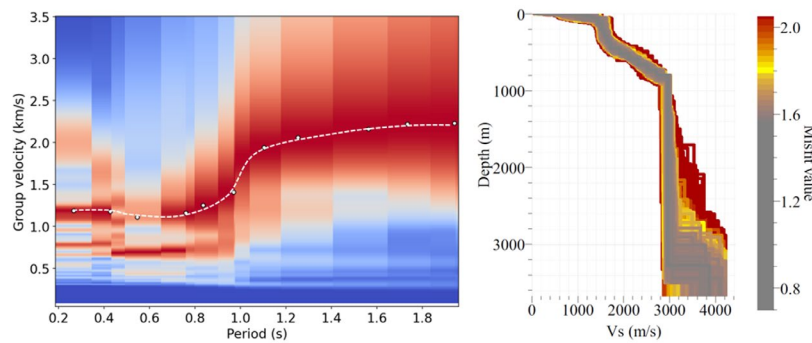


Figure 9: Left: Dispersion diagram of Rayleigh wave group velocity extracted from ANCs computed at Patua. Right: 1-D shear wave velocity (V_s) inversion using the group velocity dispersion curve (white dashed curve).

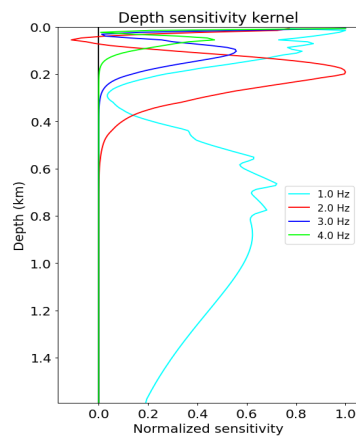


Figure 10: Depth sensitivity kernel computed using the best fitting 1-D V_s model from Figure 9.

Figure 11 shows results obtained from coda waves reconstructed between co-located surface and borehole stations. Compared to results obtained from a pair of stations at different locations, dt/t in Figure 11 are more sensitive to structures surrounding the analyzed site, i.e., velocity changes localized near the co-located sensors. Similar to those obtained from Figure 8, clear long-term linear trends are observed at different frequency bands and sites. However, there are some discrepancies between the linear trends observed in dt/t obtained from co-located sensors and pairs of sensors at different locations (e.g., velocity generally decreases for all frequency bands at station

5230). To better understand the observed spatial and temporal patterns of dt/t , we will compare dt/t curves with other datasets, such as surface deformation (e.g., Figs. 11-12) and production data.

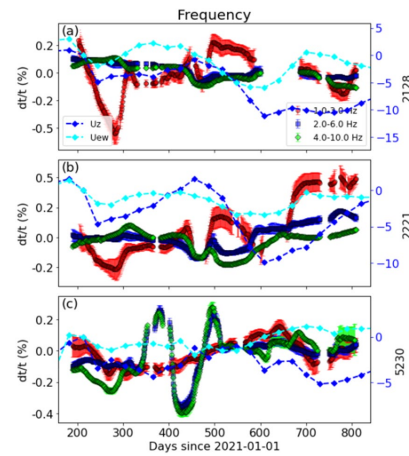


Figure 11: Comparison of dt/t curves at different frequency bands obtained from co-located borehole and surface stations. Dotted curves depict the InSAR surface deformation.

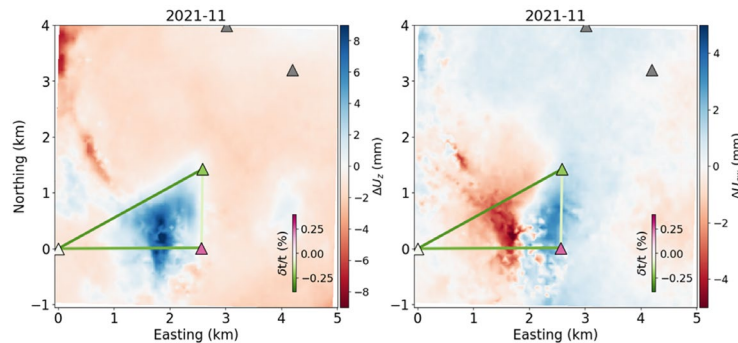


Figure 12: Comparison between the InSAR surface deformation and dt/t measurements in space.

5. GPS and InSAR

In order to understand the stress state and the changes in stress we are monitoring the regional and local deformation and strain around the geothermal field. The primary sources of data are long-term time series from the Global Positioning System (GPS) and shorter-term interferometric synthetic aperture radar (InSAR) measurements from the Sentinel-1 satellite system. The GPS network is regional in scope and the stations are outside of the Patua geothermal field (Figure 13).

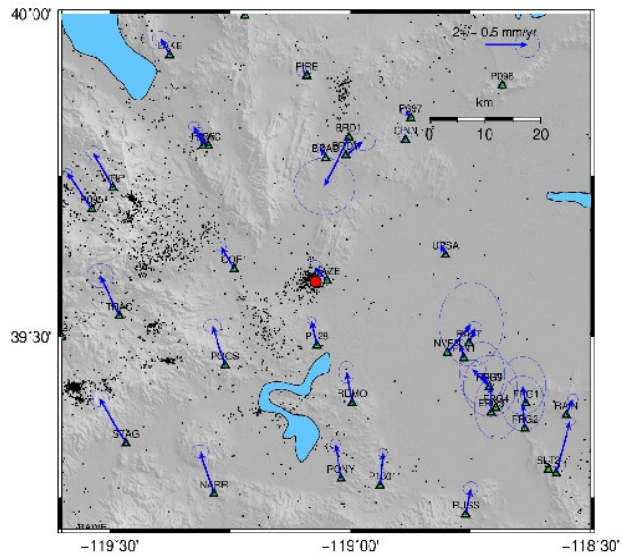


Figure 13: Global Positioning System (GPS) stations in the region surrounding the Patua field (Blewitt et al., 2018). The red dot denotes the location of the field. The blue arrows signify the horizontal displacement.

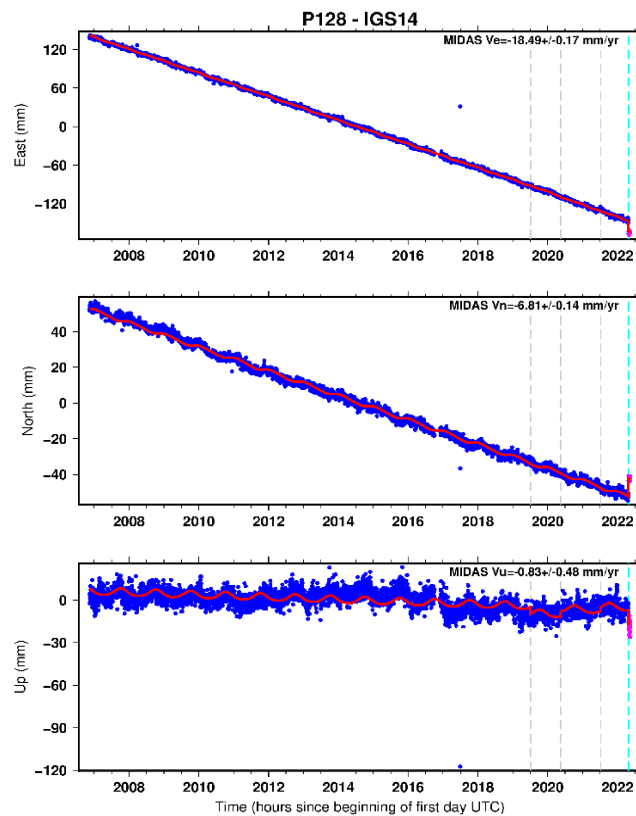


Figure 14: Three components of displacement between 2007 and 2022 for the GPS station P128.

The data have been processed by the Nevada Geodetic Laboratory and the displacements are referenced to a stable North American datum. We have changed the reference point by subtracting the displacement at station P098, which lies in the upper right corner of Figure 13. The long-term deformation is dominated by horizontal tectonic motion as may be seen by considering the three components of displacement at station P128, located about 10 km south of the Patua geothermal field.

The network of GPS stations will be used to determine the regional strain accumulation due to tectonics and will help in determining stress changes due to tectonic loading. We also need to estimate the deformation and stress changes associated with geothermal activities such as injection and production in order to evaluate fracture geometries and permeable pathways in the reservoir, as well as the potential for induced seismicity. Interferometric Synthetic Aperture Radar (InSAR) is a high-resolution technique for estimating surface displacements over time. Satellites make passes over the area of the Patua geothermal field with increasing frequency.

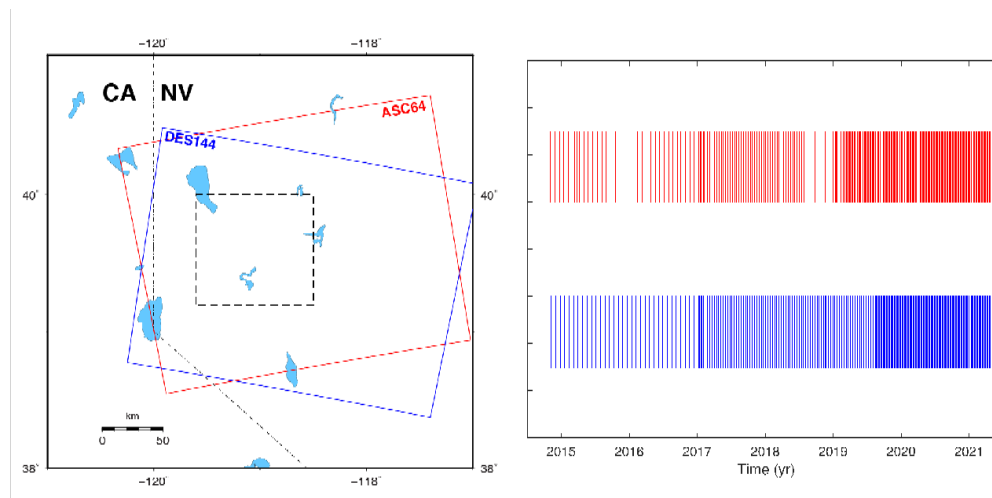


Figure 15: (Left) Ascending track ASC64 and descending track DES144 cover the region encompassing the Patua geothermal field. (Right) The temporal distribution of both tracks as they encounter the area around the geothermal field are denoted by vertical lines. The return time has been reduced to 6 days.

The satellite return time has decreased to 6 days which improves both the temporal resolution of changes and allows for more accurate estimates of displacements over each interval. Using both ascending and descending orbits it is possible to estimate both the vertical and east-west components of surface displacement. For example, in Figure 16, we plot these two components of displacement that occurred between 2018 and 2022.

One difficulty in the Patua area is the significant shallow hydrological signal that dominates the western portion of the area in Figure 16. This is not uncommon in many areas of interest containing either natural or man-made systems such as hot springs or agricultural areas. To get a feel for the magnitude of the problem and a possible solution, consider a transect across the region, as shown in Figure 17. One method that is suggested by the differences in spatial wavelengths of the anomalies in Figure 17 involves wave-number or spatial frequency filtering. That is, deeper sources, such as those in the reservoir some 2 km deep should only have long wave-length surface expressions. As an example, consider the surface deformation associated with the expansion of a single compact grid block at a depth of 2 km, an approximation of an impulse response. The surface deformation and its corresponding wavenumber spectrum are plotted in Figure 18.

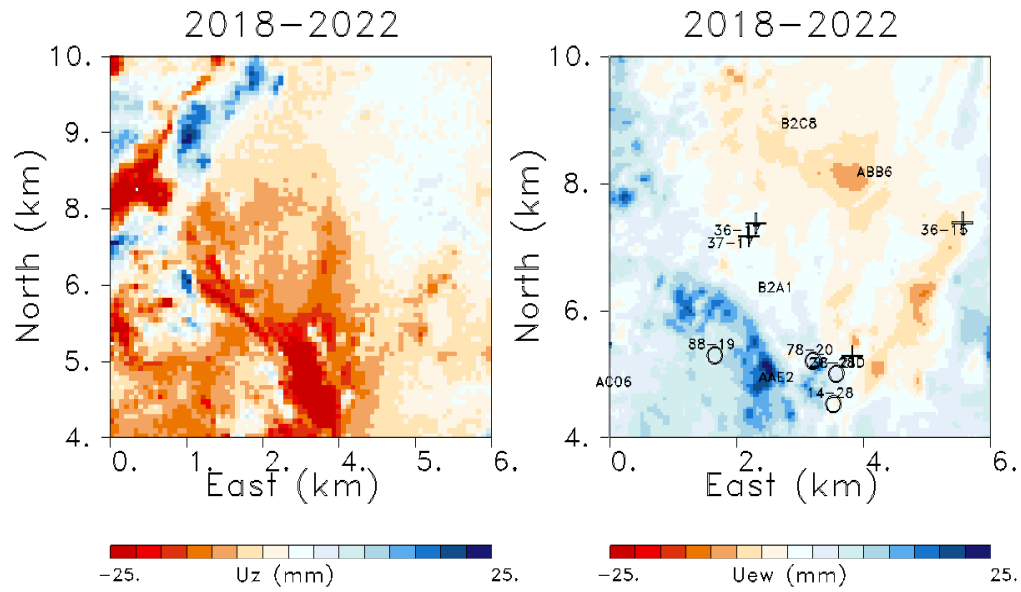


Figure 16: (Left) Vertical displacements between 2018 and 2022. (Right) East-west displacements for the same time interval. Production wells are denoted by open circles and injection wells by crosses.

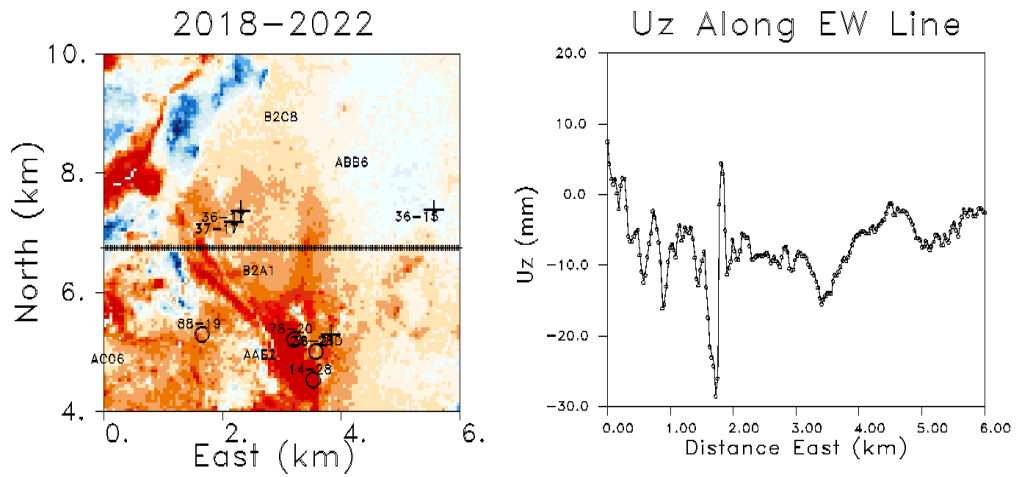


Figure 17: (Left) East-west oriented line over which the vertical displacements are sampled. (Right) Vertical displacement along the line shown in the panel on the left. Note the change in character between changes in the west and in the east.

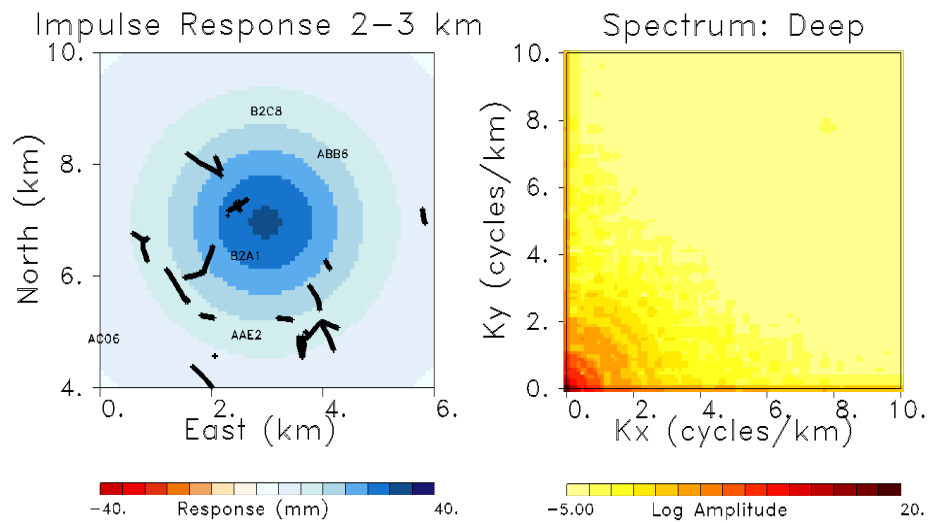


Figure 18: (Left) Surface deformation associated with the volume expansion of a single grid block at a depth of 2.0 km. (Right) Wavenumber spectrum of the anomaly plotted in the left panel.

Such deep sources should have surface wave-lengths of the order of their depth and thus the spatial wave-numbers should be relatively low. The wave number spectrum supports that contention with the largest amplitudes mostly below 2 cycles/km. For comparison we can calculate the spectrum of the vertical deformation shown in Figure 17. In the right panel of Figure 19 we display the wave number spectrum of the vertical displacement field. Note the wider distribution of energy within the spectrum to much higher wave numbers.

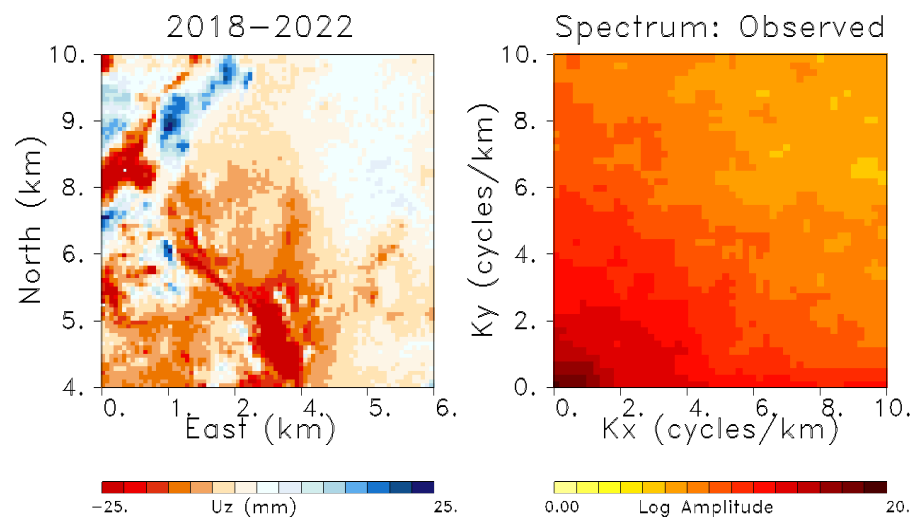


Figure 19: (Left) Observed vertical deformation obtained from the Sentinel-1 InSAR satellite system. (Right) Wave number spectrum of the displacement field.

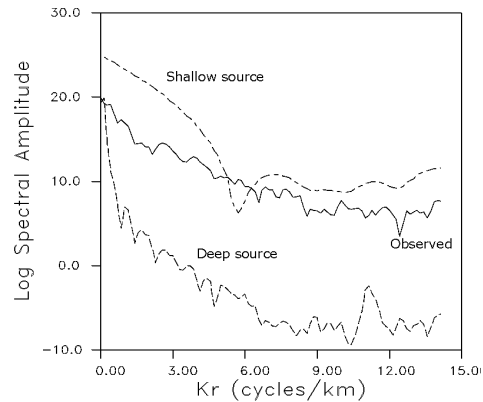


Figure 20: Radial distribution of energy for the wavenumber spectra of displacements due to a deep source, a shallow source, and the actual observations.

For a simple comparison we can compare the radial distribution of energy for a shallow source (10-300 m), a deeper source (>2000m), and the observed data (Figure 20). We see that the observed spectrum has higher wavenumbers compatible with both deep and shallow sources. Thus, there appears to be a separation in frequency and we can design a filter to remove frequencies that are expected to be small for a source at a depth of around 2 km. We implemented such a filter and applied it to the vertical deformation field shown in Figure 16. The resulting displacement field is plotted in Figure 21 along with the filtered east-west displacement field.

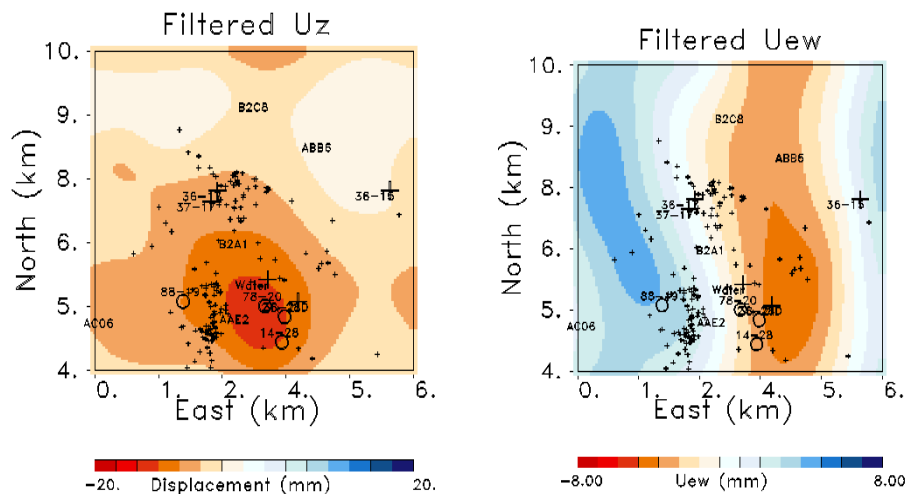


Figure 21: (Left) Vertical displacement field that results from applying a low-pass wave number filter to the observations shown in Figure 16. (Right) Corresponding east-west displacements after filtering the original displacement field.

We can now invert the filtered displacements for volume change at the reservoir depth and try to image the deformation that is induced by injection/production related processes such as poroelastic effects, thermal expansion and contraction, and other effects. We are only estimating the resulting volume change that is produced by these processes, without inferring the exact source of the deformation at this stage. Later we can compare the estimated volume changes with those due to thermal-hydrological-mechanical-chemical modeling, as described below. The inversion method

has been described elsewhere (Vasco et al., 2019, Smith and Vasco, 2020) and will not be discussed here. The estimates of volume change for a distribution of grid blocks in a model containing two layers is shown in Figure 22. Then we estimate the horizontal stress, which is the magnitude of compression/extension along the maximum horizontal stress.

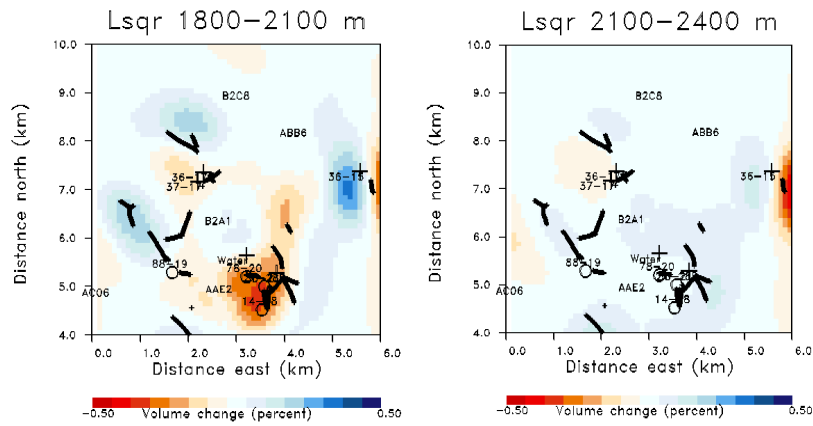


Figure 22: Estimates of volume change distributed in a model of the reservoir. The model is composed of an array of grid blocks distributed in two 300 m thick layers.

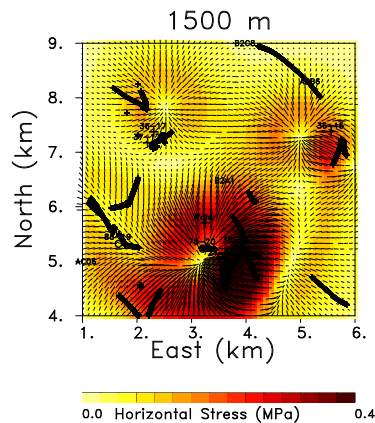


Figure 23: Horizontal stress at 150 m depth estimated from the volume changes. The short black line shows the direction of the maximum horizontal stress.

As noted above, these estimates of reservoir volume change can be compared with numerical modeling and used to update the reservoir model in an iterative fashion. They can also be used as sources for a geomechanical code to forward model the estimated deformation and stress changes due to reservoir processes. Given the favorable temporal sampling of the Sentinel-1 satellite system we can compute the stress changes for 6-day intervals in many cases. Thus, we can use the estimated stress changes to calculate velocity changes that might be observed by seismic interferometry for the deeper travel paths that are influenced by changes in the reservoir.

6. Laboratory Tests

Laboratory rock mechanics tests were performed on core from the Patua reservoir to inform static and dynamic moduli used for THMC modeling and characterize the anelastic response of reservoir material to stress changes. The core material is a medium grained, quartz-rich plutonic rock with

fractures throughout (Figure 24a). A 1.50" diameter sample for testing was sub-cored from the original core and the ends ground flat and parallel. The final core was 2.41" in length and had one significant fracture at approximately 45 degrees from the cylinder's axis. The core was oven dried and weighed and had a dry bulk density of 2.57 g/cc.

The core was placed between endcaps with integrated ultrasonic sensors and jacketed with Viton tubing. The sample was then loaded into a triaxial deformation apparatus for testing. During the experiment the axial and radial sample displacement was measured with LVDT's, the confining pressure was measured with an electronic pressure transducer and differential stress was measured with an internal load cell. The sample was first subjected to a hydrostatic sample seating procedure to ensure data quality then brought to 20 MPa confining pressure. The sample was allowed to mechanically equilibrate then an ultrasonic measurement was taken. The collected waveforms are presented in Figure 24b. After ultrasonic measurement, the confining pressure was oscillated with an amplitude of 5 MPa to measure the static bulk modulus. To measure the shear modulus, the differential stress was oscillated with an amplitude of 5 MPa while the confining pressure was decreased to maintain a constant mean stress.

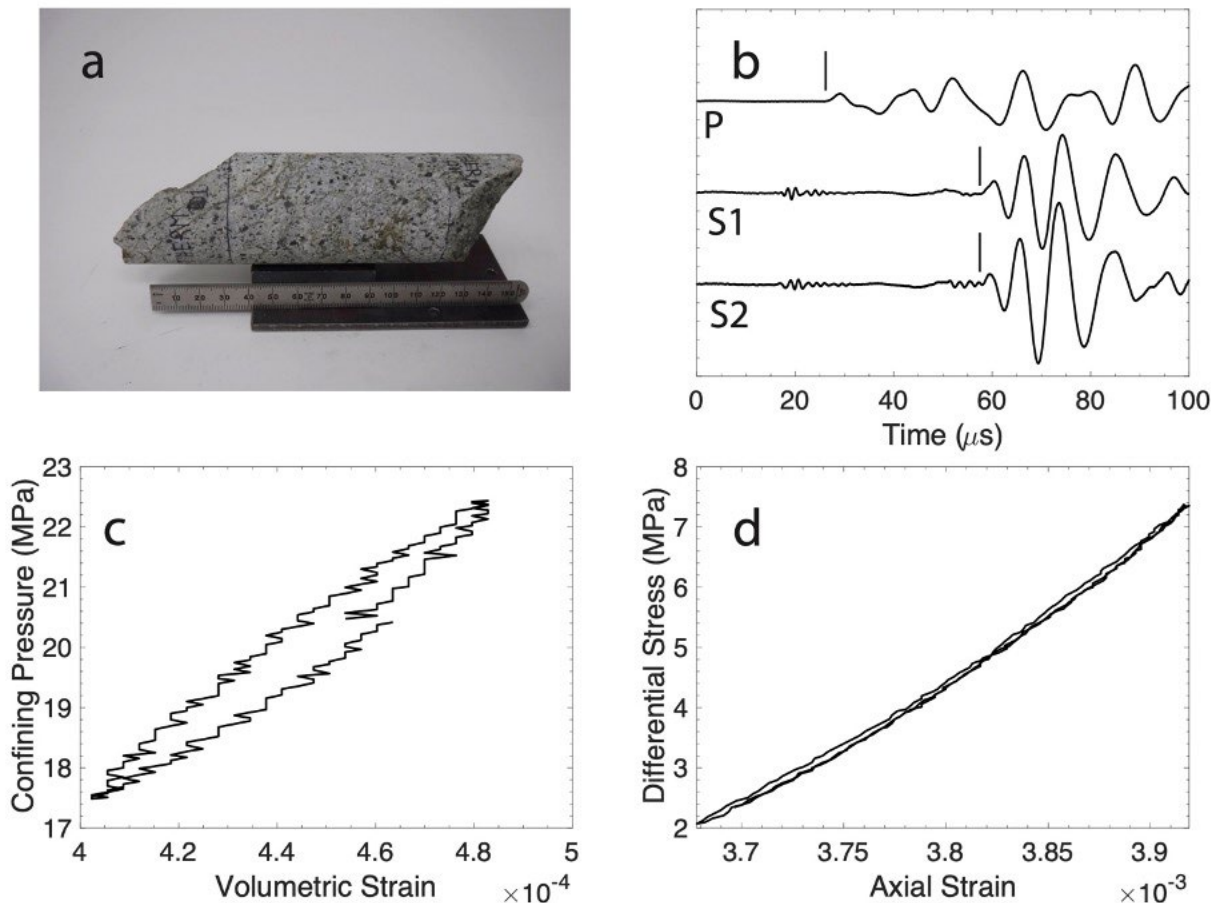


Figure 24. Data from laboratory tests of granitoid material from Patua reservoir. a) Core image of material used for testing. b) Waveforms collected from ultrasonic test of material, c) volumetric strain versus confining pressure from a bulk modulus measurement, and d) axial strain versus differential stress from a shear modulus measurement.

Sample displacements were used to calculate axial and radial strains which in turn are used to calculate volumetric and shear strain. Stress-strain curves from static modulus measurements are presented in Figure 24c and d. Travel times for P-wave and two S-waves are picked from first arrivals and used to calculate wave velocities. The wave velocities and sample density are used to calculate dynamic moduli. Static and dynamic bulk and shear moduli are reported in Table 1.

The values of static moduli are somewhat lower than those reported by Kc et al. (2019) for the same material. Closer look at the constitutive behavior of the material strongly suggests this is due to the presence of fractures in our sample. The response of our sample to hydrostatic loading is hysteretic, indicated by the open elliptical shape of the volumetric strain-confining pressure curve. Additionally, the axial strain-differential stress curve is non-linear with a convex upwards shape, indicating some strain hardening. These behaviors strongly suggest crack closure is still playing a significant role in the mechanical response of the sample at these conditions. The data suggest that the presence of fractures within the granitoid body at Patua can reduce elastic moduli and result in nonlinear, hysteretic constitutive behavior and provide context for parameter selection for THMC modeling.

Table 1. Recovered elastic properties of sample at 20 MPa confining pressure.

Property	Value
Density (g/cc)	2.57
Static Bulk Modulus (GPa)	31.2
Static Shear Modulus (GPa)	14.9
Dynamic Bulk Modulus (GPa)	35.0
Dynamic Shear Modulus (GPa)	23.2

7. THMC Modeling

We analyzed fault picks from well logs (Pollack, 2021) combined with drilling lost circulation zone (LCZ) observations (Cladouhos et al., 2017) to find a set of 12 planar segments maximizing a weighting of the number of fault picks and LCZ picks within a 25 m tolerance of the plane segments, fitting 69 of 76 data points, to determine fault geometry, shown in horizontal section at reservoir depth (1107 elevation, ~2250 m depth) in Figure 25. Starting from permeabilities similar to those of Garg et al. (2017) and Murphy et al. (2017) we adjusted them to roughly fit interpolated native state temperature data at two levels. 1107 m elevation (~150 m depth) and 1005 m below sea level (2250 m depth), and a 2013 well injection test from Garg et al. (loc. cit.).

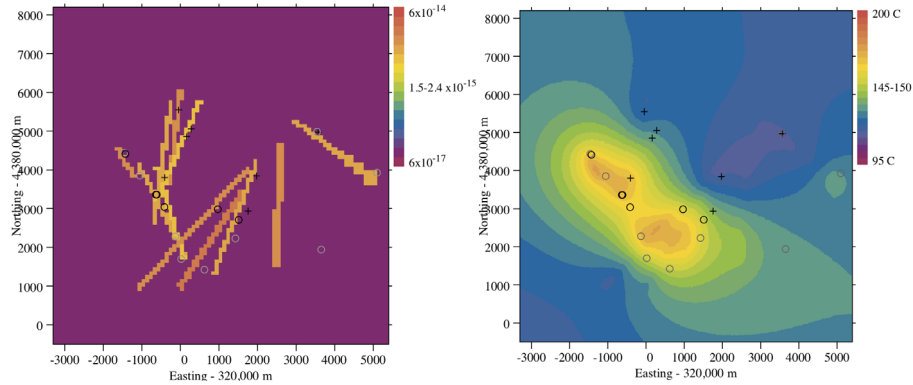


Figure 25: Left: Plan view of vertical permeability at -1005 m elevation. Right: Simulated native state temperatures at -1005 m elevation. Circles: production well head locations, crosses: injection well head locations.

As operations data became available, we considered 9 years (2013-22) of data, averaging pressure and rate data over a wide range of interval lengths, from which weekly averages were chosen as fairly representative. Pressure in lines to injection wells, injection rates, pressures at downhole sensors (bubblers) in production wells, and production rates were available. A scatter plot of line pressure as a function of injection rate is shown in Figure 26 (left). For wells 38-12, 37-17, 23-17, 36-17, 44-21, and 36A-15, there is a tendency for points to cluster about a line or multiple lines of constant slope. Lines were fit by eye, and slope interpreted as reciprocal injectivity (Pa-s/kg). For wells 85-19, and 24-29, trends were assumed to pass through the origin and also fit by eye. A scatter plot of change in downhole pressure from hydrostatic as a function of production rate is shown in Figure 26 (right). Reciprocal injectivities were determined from the ratio of pressure change to injection rate at point cluster centers.

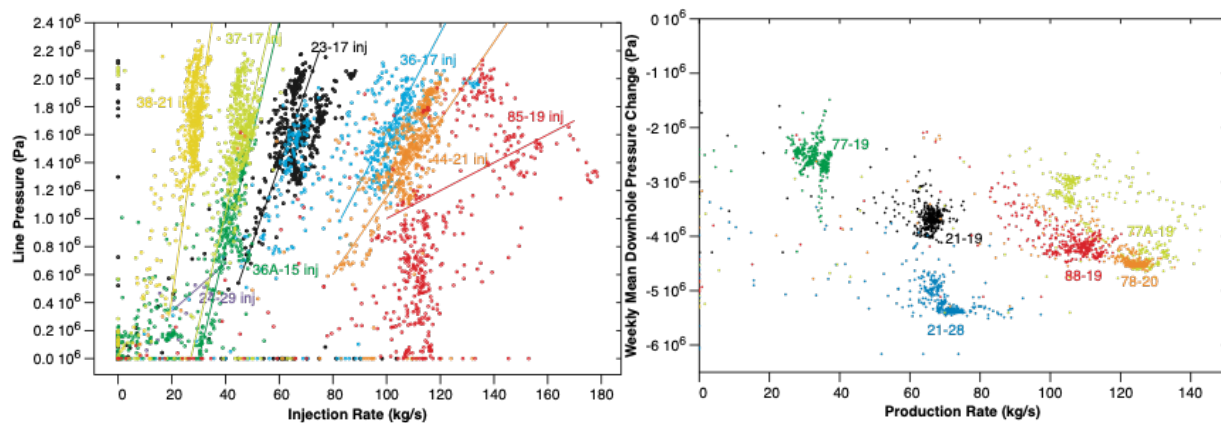


Figure 26: Left: weekly average injection well line pressure vs injection rate. Right: weekly average down hole production pressure relative to hydrostatic pressure, vs production rate.

The permeability model calibrated against the native state temperature data, and Garg et al. pressure test data, was used to simulate 1.6 years operation, using 9 year average injection and production rates. In Figure 27 (left), simulated pressure change at 1.6 years are plotted as a function of estimated (or extrapolated) pressure change, where, for injection wells, the extrapolated pressure change is the product of the injection rate and the estimated reciprocal injectivity. Two production and one injection wells show about a 4 MPa discrepancy. To better fit the operations data, partial derivatives of pressure change over 10 years operation with respect to fault unit average $((K_{xx}+K_{yy}+K_{zz})/3)$ permeability of the different fault plane segments, and with respect to the background reservoir permeability, were computed numerically. Estimated or extrapolated pressure change data was inverted for fault unit average permeability, subject to a somewhat arbitrary $0.33 \times 10^{-19} \text{ m}^2$ lower bound on average permeability. Ratios of K_{xx}/K_{zz} , K_{yy}/K_{zz} were held at values from the preliminary calibration to native state and the injection test data. Simulated pressure changes at 10 years are plotted as a function of estimated or extrapolated pressure change in Figure 27 (right). Fit to estimated or extrapolated pressure change is improved.

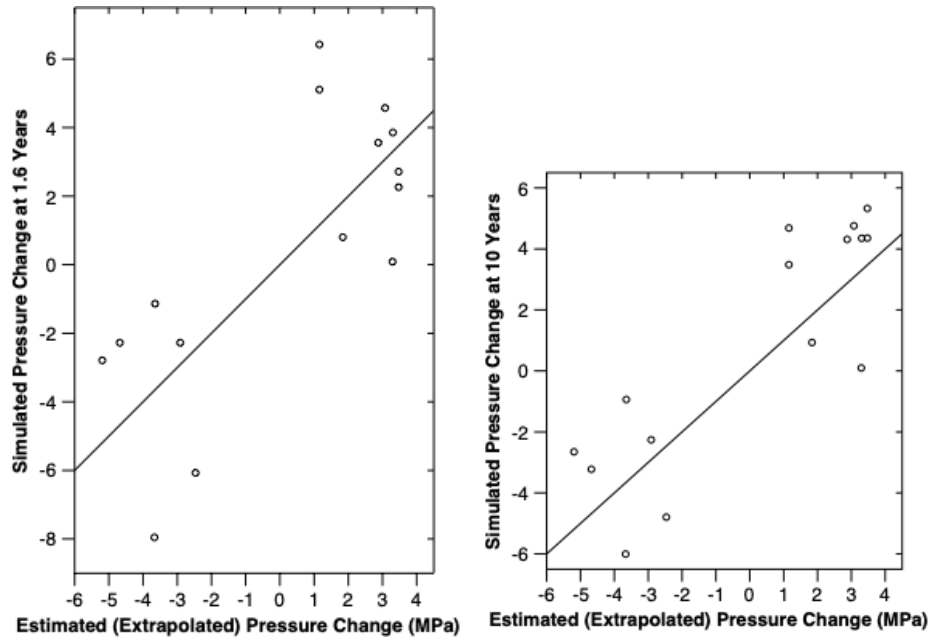


Figure 27: Left: simulated well element pressure change over 1.6 years vs estimated or extrapolated well pressure change for model from native state calibration. (negative: production well, positive: injection well). Right: simulated well element pressure change over 10 years vs estimated or extrapolated well pressure change for model with inverted permeabilities.

A horizontal section of the re-calibrated permeability model and a temperature section are shown in Figure 28. Seven of the fault segments crossing -1007 m elevation remain above the back ground permeability.

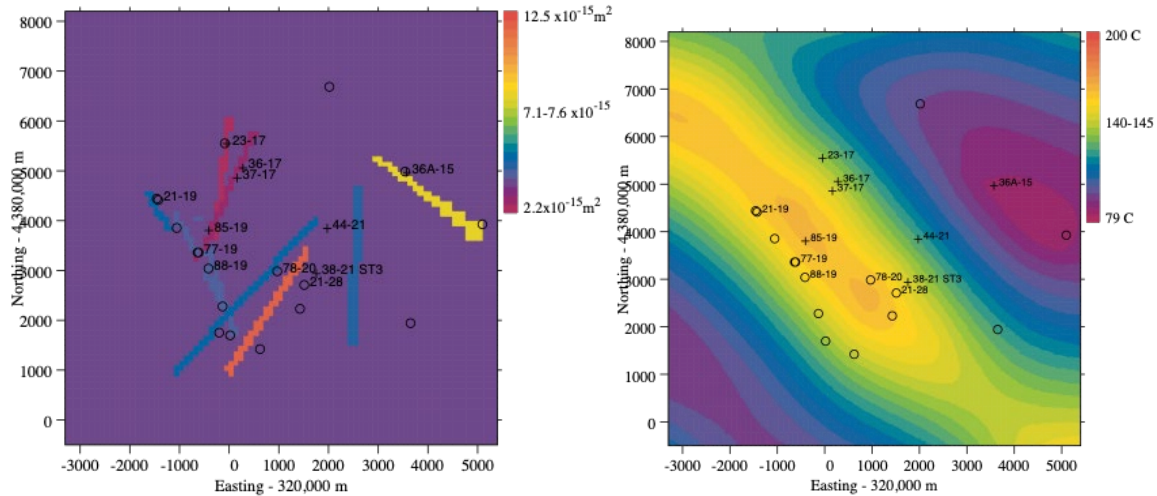


Figure 28: Left: Re-calibrated average permeability at -1007 m elevation. Right: Simulated native state temperature at -1007 m elevation in re-calibrated model.

Starting from well logs, we have averaged mechanics parameters such as density bulk and shear modulus, and scaled them to match at the depth of greatest compressional wave velocity, lower frequency measurements on core from Climax stock granodiorite (Stowe, 1969), and subsequently estimated Biot coefficient. Starting from a stress ratio estimate of 0.79: 0.53: 1 from nearby Fallon Air Force Base (Blanksma et al., 2018) we have initialized a stress model, which resolves to a model with higher horizontal stress to vertical stress in declivities, and higher in promontories. Cross sections through Northing 4,383,050 m are shown in Figure 29. Using Mohr-Coulomb fracture criteria the resultant stresses require significant material cohesion to avoid near surface failure. Preliminary efforts at modelling history production at Patua indicates minor creep at depth on existent faults.

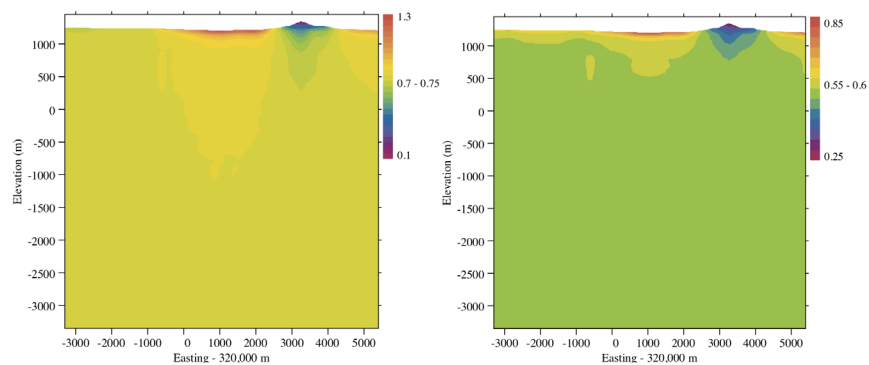


Figure 29: Left: Vertical section of ratio of east-west stress vertical stress at 4,383,050 m Northing. Right: Vertical section of ratio of north-south stress to vertical stress.

8. Conclusions

We present the current effort of stress characterization at the Patua geothermal field with seismic data acquisition, seismic ambient-noise analysis, InSAR geodesy analysis and volume change inversion, and THMC modeling. We have deployed 5-6 short-borehole seismometers at the geothermal field and measure ground motion continuously. The seismic data observed by these sensors are core information for our seismic interpretation. Surface waves in the continuous recordings provide the average 1-D V_s profile, and then based on the 1-D profile, we measure stress loading at the structure above the reservoir based on the velocity changes (dt/t). These velocity changes have spatial correlation with volumetric changes at the reservoir estimated from surface deformation in InSAR signals after isolating the long-wavelength deformation. The volume changes are concentrated at the area close to the geothermal plant. Local faults control the discontinuity of the stresses at the subsurface, based on the THMC modeling, but the reservoir changes obtained by InSAR and seismic signals are partly modeled.

9. Future Plan

In the forthcoming phase of geothermal field testing, the implementation of distributed fiber optic sensing (DFOS) will be employed with distributed thermal, strain, and acoustic signals in a monitoring well, aiming to investigate subsurface stress and strain within the geothermal field. DFOS possesses the capability to function as a distributed seismic sensor, enabling the acquisition of highly precise measurements pertaining to seismic activity across the entire extent of the fiber optic cable. Consequently, this facilitates the meticulous detection and characterization of microearthquakes, and affords valuable insights into subsurface stress and strain through the utilization of distributed acoustic sensing. By utilizing the fiber optic cable, with combining with short-borehole and surface seismometers, microearthquake occurrences can be detected and accurately localized, thereby facilitating the identification of fault structures and their spatial distribution. Furthermore, the distributed strain sensing component can effectively detect stress and strain near the monitoring well, thereby contributing to the monitoring and evaluation of fracturing development resulting from geothermal activities. The recorded data can subsequently be incorporated into THMC modeling, thereby enhancing its accuracy and optimizing well stimulation strategies, while concurrently reducing the risk associated with larger seismic events.

Acknowledgement

We are grateful to Cyrq Energy Inc. for their collaboration to this work. The seismic and well-log data are provided by the DOE Geothermal Technologies Office Wells of Opportunity Amplify project. This work is supported by the U.S. Department of Energy, Office of Energy Efficiency and Renewable Energy (EERE), Geothermal Technologies Office, under Award Number DE-AC02-05CH11231 with Lawrence Berkeley National Laboratory.

REFERENCES

- Bensen, G.D., Rizwoller, M.H., Barmin, M.P., Levshin, A.L., Lin, F., Moschetti, M.P., Shapiro N.M., and Yang, Y.: Processing seismic ambient noise data to obtain reliable broad-band surface wave dispersion measurements, *Geophys. J. Int.*, 169, (2007), 1239–1260.
- Blanksma, D.J., Blake, K., Pettitt, W., Sabin, A., Varun V., and Damjanac B., 2018. Using Borehole Induced Structure Measurements at Fallon FORGE Combined with Numerical Modeling to Estimate In-Situ Stresses, *Proceedings, 43rd Workshop on Geothermal Reservoir Engineering, Stanford, Calif.*
- Blewitt, G., W.C. Hammond, C. Kreemer: Harnessing the GPS Data Explosion for Interdisciplinary Science, *Eos*, (2018), 99.
- Cladouhos, T.T., Uddenberg, M.W., Swyer, M.W., Nordin, Y., and Garrison, G.H., 2017. Patua geothermal geologic conceptual model, *GRC Transactions*, Vol. 41.
- Combs, J., Peterson, N., Garg, S.K., and Gorenson, C.: Reservoir testing and analysis at the Patua geothermal federal unit, northwestern Nevada, *GRC Transactions*, 36, (2012), 31–36.
- Garg, S.K., Goranson, C., Johnson, S., and Casteel, J.: Reservoir testing and modeling of the Patua geothermal field, Nevada, USA, *Proceedings World Geothermal Congress 2015, Melbourne, Australia*, (2015).
- Kc, B., Foroutan, M., Kamali-Asl, A., Ghazanfari, E., & Cladouhos, T. T. (2019, June). Geomechanical characterization of a granodiorite rock specimen from Patua geothermal field. In *ARMA US Rock Mechanics/Geomechanics Symposium* (pp. ARMA-2019). ARMA.
- Lobkis, O.I., and Weaver, R.L.: Coda-wave interferometry in finite solids: recovery of P-to-S conversion rates in an elastodynamic billiard, *Phys. Rev. Lett.*, 90(25 Pt 1), (2003).
- Moreau, L., Stehly, L., Boue, P., Lu, Y., Larose, E., and Campillo, M.: Improving ambient noise correlation functions with an SVD-based Wiener filter, *Geophys. J. Int.*, 211, (2017), 418–426.
- Murphy, J., Holt, R., and Morrison, M.: A numerical model case study of the Patua geothermal field, *GRC Transactions*, 41, (2017).
- Smith, J.T., and Vasco, D.W.: Adjoint-based inversion of geodetic data for sources of deformation and strain, *Journal of Geophysical Research*, 126, (2021), 1-12, e2021JB021735.
- Pollack, A., Cladouhos, T.T., Swyer, M.W., Siler, D., Mukerji, T., and Horne, R.N.: Stochastic inversion of gravity, magnetic, tracer, lithology, and fault data for geologically realistic structural models: Patua geothermal field case study, *Geothermics*, 95, (2021), 102129.
- Vasco, D.W., Farr, T.G., Jeanne, P., Doughty, C. and Nico, P.: Satellite-based monitoring of groundwater depletion in California's Central Valley, *Scientific Reports*, 9, (2019), 1–14.
- Wathelet, M. (2008). An improved neighborhood algorithm: Parameter conditions and dynamic scaling. *Geophysical Research Letters*, 35, L09301. <https://doi.org/10.1029/2008GL033256>